ACS APPLIED MATERIALS & INTERFACES

Research Article

Cite This: ACS Appl. Mater. Interfaces 2017, 9, 43632−43639

www.acsami.org

Exploring Highly Reversible 1.5-Electron Reactions ($V^{3+}/V^{4+}/V^{5+}$) in $Na_3VCr(PO_4)_3$ Cathode for Sodium-Ion Batteries

Rui Liu,[†] Guiliang Xu,[‡] Qi Li,[†] Shiyao Zheng,[†] Guorui Zheng,[†] Zhengliang Gong,[§] Yixiao Li,[†] Elizaveta Kruskop,[†] Riqiang Fu,[∥] Zonghai Chen,[‡] Khalil Amine,[‡,⊥] and Yong Yang*[,†,§]

[†]Collaborative Innovation Center of Chemistry for Energy Materials, State Key Laboratory for Physical Chemistry of Solid Surface, Department of Chemistry, College of Chemistry and Chemical Engineering, and [§]School of Energy Research, Xiamen University, Xiamen 361005, PR China

[‡]Chemical Sciences and Engineering Division, Argonne National Laboratory, 9700 South Cass Avenue, Argonne, Illinois 60439, United States

[∥]National High Magnetic Field Laboratory, 1800 East Paul Dirac Drive, Tallahassee, Florida 32310, United States

[⊥]Materials Science and Engineering, Stanford University, Stanford, California 94305, United States

Supporting Information

ABSTRACT: The development of highly reversible multielectron reaction per redox center in sodium super ionic conductor-structured cathode materials is desired to improve the energy density of sodium-ion batteries. Here, we investigated more than one-electron storage of Na in $Na_3VCr(PO_4)_3$. Combining a series of advanced characterization techniques such as ex situ ^{51}V solid-state nuclear magnetic resonance, X-ray absorption near-edge structure, and in situ X-ray diffraction, we reveal that V^{3+}/V^{4+} and V^{4+}/V^{5+} redox couples in the materials can be accessed, leading to a 1.5-electron reaction. It is also found that a light change on the local electronic and structural states or phase change could be observed after the first cycle, resulting in the fast capacity fade at room temperature. We also showed that the irreversibility of the phase changes could be largely suppressed at low temperature, thus leading to a much improved electrochemical performance.

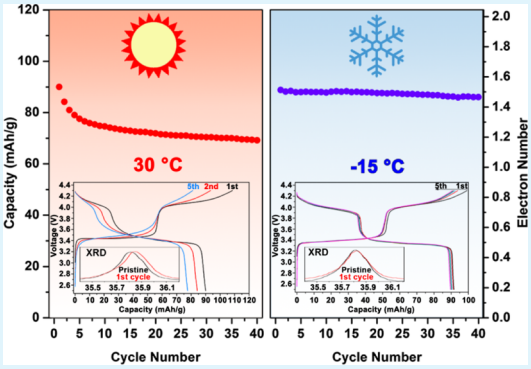

KEYWORDS: *sodium-ion batteries, multielectron reaction, NMR, XAS, structural evolution, low temperature, NASICON*

INTRODUCTION

Lithium-ion batteries (LIBs) have dominated in mobile energy storage, and they are being considered as the most promising technology for pure and hybrid electrical vehicles and smart grid. However, the ever-growing demand for Li salt poses great challenges on the reserves of Li resources in the earth crust and pushes up the costs of LIBs. As a result, it is necessary to find low-cost alternatives of LIBs. Sodium-ion batteries (SIBs) would be one of the best choices for the stationary energy storage owing to the natural abundance and low cost of Na resources. Polyanionic phosphates served as the cathodes for SIBs have aroused an extensive consideration owing to their stable structure and safety but have not been fully successful because of their low capacity.[1−3] Accessing more than one-electron reactions in the cathodes could in principal increase both the capacity and the potential of the electrodes and is highly accessible based on the multiple redox couples ($M^{n+}/M^{(n+1)+}$ and $M^{(n+1)+}/M^{(n+2)+}$) of some transition metals such as V,[4] Mo,[5] and Mn.[6]

The sodium super ionic conductor (NASICON)-structured $Na_{3+x}M1_yM2_{1-y}(PO_4)_3$ materials are excellent model materials for SIBs. At first, in a NASICON-structured $Na_{3+x}M1_yM2_{1-y}(PO_4)_3$, M1 and M2 are generally first-row transition metals, and y could be freely adjusted, leading to the statistically distributed M at the 12c site and enabling versatile redox centers in the structure. Second, there are two crystallographic sites of Na, 6b Na(1) site and 18e Na(2) site with the amount of Na in the structure reaching a maximum of four per formula unit, which allows multiple Na extraction and insertion. Goodenough's group has prepared NASICON-structured $Na_3MnTi(PO_4)_3$ which exhibited two voltage plateaus at 3.6 and 4.1 V versus Na^+/Na owing to the redox couple of Mn^{2+}/Mn^{3+} and Mn^{3+}/Mn^{4+}, respectively.[6] Besides, Masquelier's group has investigated the electrochemical properties and phase transition of $Na_3Al_{0.5}V_{1.5}(PO_4)_3$.[4] When charged to 4.2 V versus Na^+/Na, two voltage plateaus located at ∼3.4 and ∼4.0 V have been observed, involving the redox couple of V^{3+}/V^{4+} and V^{4+}/V^{5+}, respectively. In addition, Yamada et al. have also accessed Fe^{2+}/Fe^{3+}, V^{3+}/V^{4+}, and V^{4+}/V^{5+} redox couples during charge/discharge through introducing

Received: August 28, 2017
Accepted: November 22, 2017
Published: November 22, 2017

DOI: 10.1021/acsami.7b13018
ACS Appl. Mater. Interfaces 2017, 9, 43632−43639

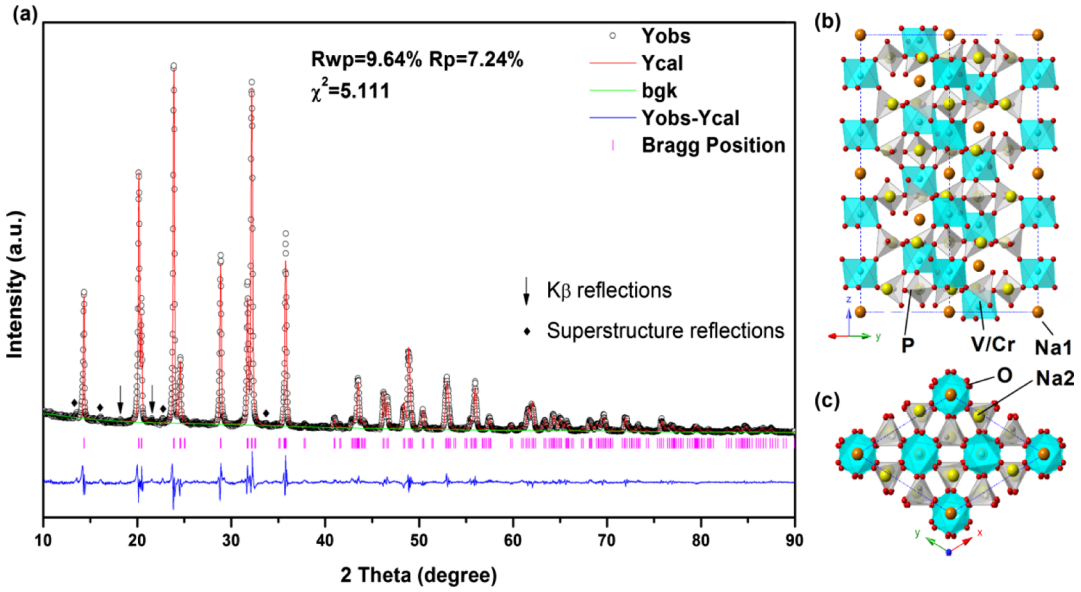

Figure 1. (a) XRD pattern and Rietveld refinement of NVCP. The arrows indicate residual Cu Kβ peaks caused by the diffractometer. The diamonds indicate superstructure reflections. (b,c) Schematic representation of the NVCP structure.

excessive Na into the NASICON structure to form $Na_{3.5}V_{1.5}Fe_{0.5}(PO_4)_3$.[7] In addition to these studies, extensive investigations have been conducted involving the partial substitution of V by Mn,[8] Al,[9] Fe,[10] and Cr[11] in $Na_3V_2(PO_4)_3$, in which the activation of V^{3+}/V^{4+} and V^{4+}/V^{5+} has been observed.

However, the maximum number of electrons involved in the electrode reaction from all of the reported results is less than 1 per vanadium ion, and the cycling performance is unsatisfactory.[4,7] Consequently, it is important to improve the reacted number of electrons per vanadium ion and to elucidate the reason of the capacity fading. Herein, we used $Na_3VCr(PO_4)_3$ (NVCP) as the model material because the inactive Cr^{3+} in the common voltage window (2.5−4.3 V vs Na^+/Na) enables to solely study the multielectron reaction of vanadium.[11] Moreover, the crystal radius of Cr^{3+} (0.755 Å) similar to that of V^{3+} (0.78 Å) would allow the statistic distribution of V^{3+} and Cr^{3+} in NVCP.[11] Combining ^{51}V solid-state nuclear magnetic resonance (ss-NMR), X-ray absorption spectroscopy (XAS), in situ and ex situ X-ray diffraction (XRD), and the standard electrochemical measurement, we revealed a 1.5-electron transfer in NVCP with an asymmetric reaction pathway for electrochemical reactions. Besides, we further proposed that the deep desodiated species $Na_{2-y}V_y^{5+}V_{1-y}^{4+}Cr(PO_4)_3$ is metastable, which induces the irreversibility of the phase transformation at 30 °C. By suppressing the irreversibility at low temperature, we are able to achieve an excellent reversible 1.5-electron $V^{3+}/V^{4+}/V^{5+}$ cycling.

EXPERIMENTAL SECTION

For the synthesis of NVCP/C, we used a method similar to that reported by An et al.[12] In particular, 1 mmol of V_2O_5, 2 mmol of $Cr(NO_3)_3{\cdot}9H_2O$, and 6 of mmol $H_2C_2O_4{\cdot}2H_2O$ were dissolved in 20 mL of deionized water. The solution was magnetically stirred for 1 h at 70 °C and then 6 mmol of $NaH_2PO_4{\cdot}2H_2O$ and 0.2 g of glucose were added, and the mixture was stirred for another 5 min. Subsequently, 50 mL of *n*-propanol was added into the solution and stirred for 10 min to form a sol, which was then dried in an oven to get a gel. The final product was obtained by heating the gel at 400 °C for 4 h and then at 750 °C for 8 h (5 °C/min) in a tube furnace in an Ar atmosphere. The product was denoted as NVCP for short.

The carbon content of the product was determined with a Vario EL III elemental analyzer (Elementar AnalysenSystem GmbH, Germany), and the value is approximately 2% according to which the specific content of the active material in the composite electrode was corrected.

Ex situ XRD patterns were collected with a Rigaku Ultima IV powder X-ray diffractometer using Cu Kα radiation (λ = 1.5406 Å) operated at 40 kV and 30 mA from 2θ = 10 to 90° at a scan speed of 4°/min. Rietveld refinement of the XRD pattern was performed using a GSAS code. The scanning electron microscopy (SEM) images were obtained using a Hitachi S-4800 scanning electron microscope with an energy-dispersive X-ray spectroscopy (EDS) detector used for EDS elemental mapping.

In situ synchrotron XRD was carried out at Sector 11-ID-D of the advanced photon source of Argonne National Laboratory, with the wavelength of X-ray used preset to 0.1173 Å. A coin cell with holes at both top and bottom which were sealed with a Kapton tape was used for the in situ charge and discharge. During the in situ measurements, the cell was continuously charged and discharged and the data collection time for each XRD scan was 14−15 min.

The ex situ XAS data at the V and Cr K edges were collected in a transmission mode at room temperature, using ion chamber detectors at beamline BL14W1 of the Shanghai Synchrotron Radiation Facility and a Si(111) double-crystal monochromator. The data were collected over a range of energies, from 200 eV below to 500 eV above the V (5465 eV) and Cr (5989 eV) K edges, respectively. The incident photon energy was calibrated using a standard V metal foil. Processing and fitting of the XAS data were performed using Athena software.[13]

All NMR experiments were performed on a Bruker AVANCE III 400 MHz NMR spectrometer. The ^{51}V NMR spectra were acquired using 1.3 mm probehead at spinning rates of 55 kHz. A recycle delay of 2 s and a 90° pulse length of 2 μs were used for spin echo. The chemical shift of ^{51}V was referenced to V_2O_5 powder (−610 ppm).

Electrochemical experiments were carried out in 2025 coin-type cells or T-shaped Swagelok three-electrode cells. The working electrode was prepared by coating the slurry of the active materials, acetylene black, and polyvinylidene fluoride in the weight ratio of 8:1:1 using *N*-methyl-2-pyrrolidone as the solvent onto an Al foil substrate and dried overnight in a vacuum oven at 120 °C. The Na metal foil was used as the counter electrode, and a glass fiber was used as the separator. The electrolyte was composed of a solution of 1 M $NaClO_4$ in propylene carbonate (PC) and fluoroethylene carbonate (FEC)

DOI: 10.1021/acsami.7b13018
ACS Appl. Mater. Interfaces 2017, 9, 43632−43639

(98:2 by volume). The cells were assembled in an argon-filled glovebox. The cells were galvanostatically charged and discharged on a LAND CT-2001A (Wuhan, China) battery test system.

For ex situ measurements, the cells were stopped at specific points and disassembled in an Ar-filled glovebox. The positive electrodes were rinsed with PC and then with dimethyl carbonate thrice. For ex situ NMR measurements, the electrode materials were scraped carefully from the Al current collector and sealed in the probehead in the glovebox. For ex situ XAS tests, the electrode materials were unstuck from the Al current collector and then sealed by the Kapton film. The electrodes were directly used for ex situ XRD tests with Al current collector, indicating the identity of sample processing.

RESULTS AND DISCUSSION

Figure 1a shows the XRD pattern of the as-obtained NCVP. In addition to some superstructure peaks and residual Cu Kβ peaks, all of the diffraction peaks can be indexed in a rhombohedral system with the space group of $R\bar{3}c$.[14] According to the results of the refinement, the lattice parameters of NVCP are a = 8.68951(12) Å, c = 21.7281(5) Å, and V = 1420.835 Å^3. Evidently, they are smaller than that of $Na_3V_2(PO_4)_3$ as expected from the smaller crystal radius of Cr^{3+} (0.755 Å) in comparison with that of V^{3+} (0.78 Å).[11] The detailed atomic positions of NVCP are listed in Table S1. Figure 1b,c presents the NVCP crystal structure with a NASICON framework. The octahedral VO_6 interlinks via the corners with tetrahedral PO_4 to form the three-dimensional $V_2(PO_4)_3$ lantern units that are interconnected through PO_4 with the neighboring units. Six lantern units build up the primitive cell of NVCP, in which two different oxygen environment interstitial sites exist: Na(1) with sixfold coordination and Na(2) with eightfold coordination. Na(1) locates between two adjacent $V_2(PO_4)_3$ lantern units along the z-axis, and Na(2) situates at the same z value as the P atoms between two PO_4 tetrahedra. The morphology and size of NVCP were observed using SEM, as shown in Figure S1a. Most of the particles exhibit irregular shape with the particle sizes from several to tens of micrometers. However, the high-magnification image in Figure S1b shows that the particles are formed from the agglomeration of smaller primary particles with the sizes near 500 nm. Moreover, EDS was employed to analyze the chemical composition of NVCP. Figure S1c shows that the elements of Na, P, V, Cr, O, and C distribute uniformly in the particles.

The electrochemical performance of the sample was evaluated using galvanostatic charge and discharge at 30 °C in the voltage range of 2.5−4.3 V versus Na^+/Na, which can be found in Figure 2a. Different from the well-known single plateau feature of $Na_3V_2(PO_4)_3$,[15] two pronounced plateaus and a step between these are observed during the first charge of NVCP. The dQ/dV curves at the first charge of NVCP shown in Figure 2b further demonstrate that the two voltage plateaus of the product are located at approximately 3.4 and 4.1 V. In addition, similar results have also been reported in other $Na_{3+y}V_{1-x}M_x(PO_4)_3$ (M = Al,[4,9] Fe,[7,10] Mn,[8] Cr,[11] etc.) system. Specifically, the low-voltage plateau occurs at ∼3.4 V, corresponding to the extraction of Na^+ from the structure and meanwhile the oxidation of vanadium from V^{3+} to V^{4+}. Figure 2a shows that the capacity of the low-voltage plateau fits well with one-election reaction of NVCP. After jumping over the voltage step, the voltage continuously increases from 4.0 to 4.3 V versus Na^+/Na, accompanying the oxidation of V^{4+} to V^{5+} when the second Na^+ is extracted from NVCP, reaching a charge capacity of ∼109 mA h/g. The first discharge capacity is 90 mA h/g, representing a reversible 1.5-electron reaction,

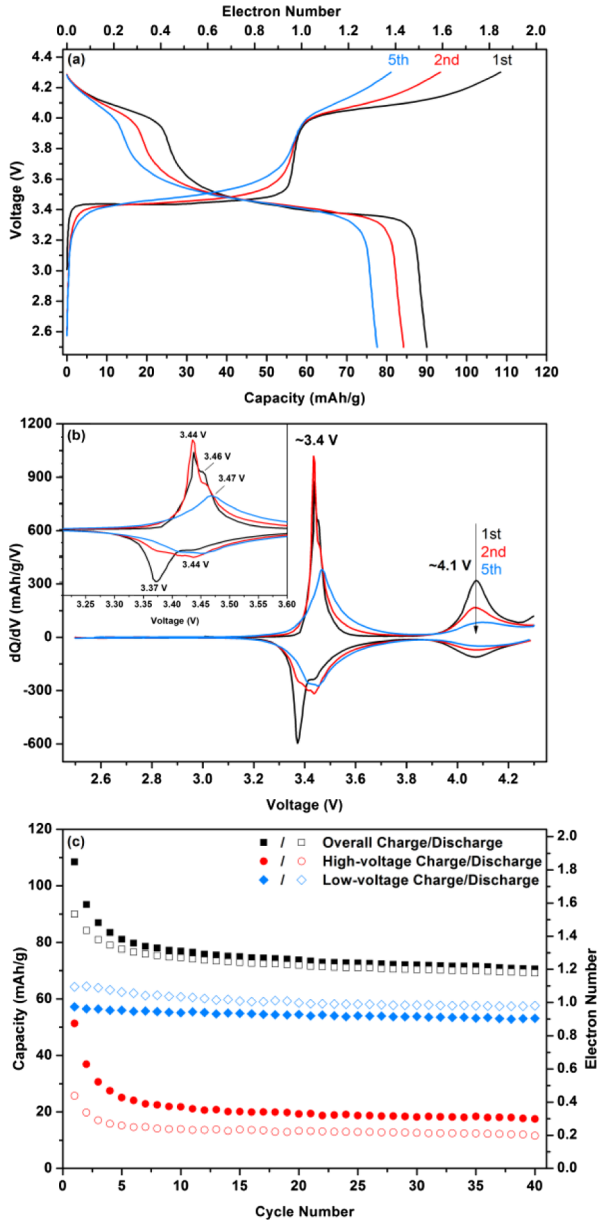

Figure 2. (a) Galvanostatic charge/discharge curves, (b) corresponding dQ/dV curves, and (c) overall, low-voltage, and high-voltage capacities versus cycle number of NVCP cycled in coin cells at 0.1 C at 30 °C.

which corresponds to an initial Coulombic efficiency of only 82.6%. Moreover, a close view of the dQ/dV curves in the inset of Figure 2b further reveals that the low-voltage region of the first charge exhibits two adjacent peaks at 3.44 and 3.46 V, which has also been proven in $Na_3V_{1.5}Al_{0.5}(PO_4)_3$ by Masquelier and the collaborators.[4]

Another feature is that the charge/discharge curves of the second and fifth cycles are evidently different from the first cycle. First, according to Figure 2a, the staircase voltage profile near the step region at the first charge converts to the S-shaped profile on the discharge process and continuously changes during the following cycles. Similar results could also be found from the dQ/dV curve; these two peaks at the low-voltage region progressively merge together accompanied with shifting to a higher-voltage region. Moreover, the charge/discharge profiles shown in Figure 2a also reveal that the voltage plateaus

DOI: 10.1021/acsami.7b13018
ACS Appl. Mater. Interfaces 2017, 9, 43632−43639

in the low-voltage region gradually increase during cycling. Similar features could be seen in the discharge process as well, indicating the discrepant Na extraction/insertion process among different cycles.

Moreover, we deliberately divided the charge/discharge curves cycled between 2.5 and 4.3 V into low-voltage and high-voltage regions, respectively. The capacity versus cycle number of the two regions is presented in Figure 2c. The overall capacity drops quickly from 90 to 77.6 mA h/g in five cycles, which is mainly due to the loss of high-voltage capacity. Furthermore, the low-voltage discharge capacity is higher than the charge capacity in the first several cycles, consistent with the smoothed feature of the voltage step.

Figure S2 shows the charge/discharge curves cycled with the upper limit cutoff voltage of 4.0 V for three cycles and subsequently to 4.1 V for several cycles at 30 °C. Obviously, if the upper limit is 4.0 V, NVCP shows a negligible capacity loss during cycling. Whereas if the upper limit is set to 4.1 V, a pronounced loss of the capacity mainly resulting from the loss of the high-voltage capacity can be observed.

The valence states of vanadium ions at different charge/discharge stages were investigated through using a synchrotron X-ray absorption near-edge structure (XANES) and ex situ ^{51}V MAS NMR. XANES is a powerful tool to understand the local structure and the oxidation state of the absorbing elements, in our case, vanadium. The pre-edge absorption is assigned to a formally dipole-forbidden transition from 1s to the unoccupied 3d orbital in an ideal octahedral symmetry. Besides, the absorption would be partially allowed in the presence of the 3d−4p orbital mixing caused by the noncentrosymmetric V−O coordination environment. Therefore, the nature and symmetry of the V−O octahedral could be represented by the intensity and position of the pre-edge absorption. In addition, the absorption edge is aroused by the 1s to 4p transition and the position of which could indicate the oxidation of vanadium ions. More specifically, the higher the energy of the edge position is, the higher the valence state of the absorption element.

To investigate the redox behavior, ex situ XANES of NVCP at different charge/discharge stages was measured at the K edge of vanadium. On the basis of 3b, the pre-edge of the original state of NVCP is composed of three peaks located at 5465.9, 5467.9, and 5469.5 eV, which are the characteristics of the V^{3+} state.[16−18] As the battery was charged to 3.8 V, that is, the end point of the low-voltage region, an absorption positioned at 5469.5 eV appears in the pre-edge absorption, which is the characteristic of a V^{4+} state.[16−18] Moreover, Figure 3a shows that the edge shifts toward a higher energy, also demonstrating the existence of V^{4+} in NVCP at the end of the low-voltage plateau. The result confirms that the low-voltage plateau from the charge/discharge curve is in relation to the one-electron V^{3+}/V^{4+} reaction. Further charging results in a strong new peak at 5470.7 eV in the pre-edge which is consistent with V^{5+}.[16−18] However, the shift of the edge indicates that V^{4+} is not completely oxidized to V^{5+} when charged to 4.3 V, which may be caused by the relatively sluggish kinetics of the active material and the competitive oxidation of the electrolyte in the high-voltage region.[6]

When discharged to 3.8 V, the absorption edge of NVCP shifts back near its corresponding charge state, indicating an average valence state of about +4 of the vanadium ions. However, the pre-edge still exhibits a considerable characteristic of V^{5+} (5470.7 eV), which indicates that a part of the vanadium

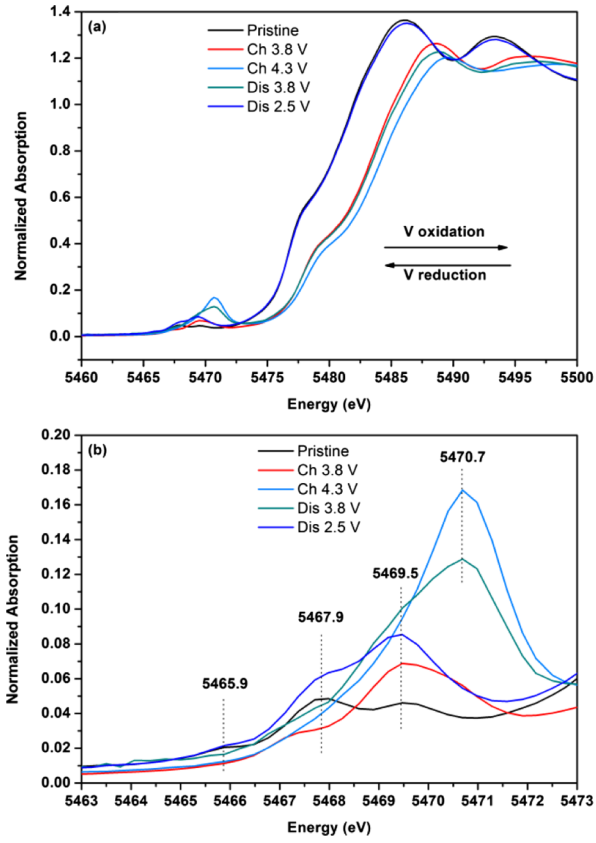

Figure 3. (a) Ex situ XANES and (b) corresponding pre-edge region at the K edge of V of NVCP charged/discharged to specific stages at 30 °C.

ions still remain in the pentavalent state, whereas a part of the vanadium ions are reduced to V^{4+} with a part being further reduced to V^{3+}, resulting in the average valence near tetravalent state when discharging the electrode to 3.8 V. As a result, we suggest that the variation of the relative amount of V^{3+}, V^{4+}, and V^{5+} species in the electrode in the voltage step region may lead to the smooth feature of the voltage step in the first discharge curve (and in the following charge/discharge process). Besides, the edge and the pre-edge peaks shift back near the original positions when further discharging to 2.5 V, implying that the valence state of vanadium ions returns to approximately trivalent state. However, the intensity of the pre-edge of the sample at the end of discharge is higher than that of the pristine one, indicating that the local environments of vanadium ions are not completely recovered. It should be noted that the valence state of Cr does not change during the charge process from XANES data at the K edge of Cr shown in Figure S3, further confirming that most of these electrochemical behaviors should arise from the redox reaction of vanadium.

To investigate the local vanadium environments in more detail during the oxidation/reduction process, the k^3-weighted Fourier-transformed vanadium using extended X-ray absorption fine structure within k = 2 to 11 $Å^{-1}$ of NVCP at various stages of charge was calculated, as shown in Figure S4. Besides, the peak around 1.5 Å is associated with the first coordination shell around the vanadium atoms, that is, VO_6 octahedral. The peaks shift to lower values in the charging process, indicating that the length of V−O bonds decreases owing to the oxidation of vanadium ions. In the discharging process, the peak position shifts back to the corresponding position of the charge process,

DOI: 10.1021/acsami.7b13018
ACS Appl. Mater. Interfaces 2017, 9, 43632−43639

yet the peak intensity changes slightly, indicating that the changes of the coordination of vanadium atoms are irreversible as well.

When using standard NMR methods, typically, only ^{51}V NMR spectra of V^{5+} compounds without localized d electron are visible.[19,20] Figure 4 shows the ex situ ^{51}V NMR spectra of

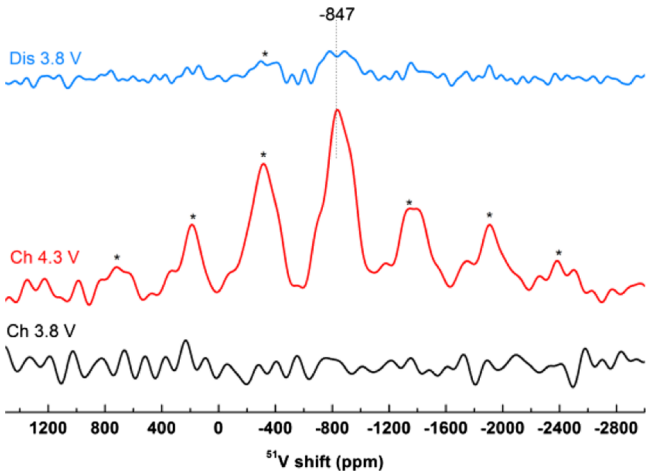

Figure 4. Ex situ ^{51}V ss-NMR of NVCP charged/discharged to specific stages at 30 °C. The symbol "*" indicates the spin side bands.

NVCP charged to 3.8 and 4.3 V and discharged to 3.8 V after being charged to 4.3 V, respectively. Notably, only noise can be observed in the spectra of NVCP charged to 3.8 V, indicating that V is not oxidized to V^{5+} at 3.8 V. After charging to 4.3 V, resonance at −847 ppm could be clearly observed, testifying the existence of a considerable amount of V^{5+} in this stage. More importantly, the resonance at −847 ppm with much more decreased intensity which could still be seen in the electrode is discharged to 3.8 V, indicating that most of V^{5+} are reduced to the lower valence state with a small amount of residual V^{5+} in the electrode. These features conform well with the XANES results.

In situ synchrotron XRD was carried out to further understand the structure transitions during the first cycle. The in situ cell was first charged to 4.3 V and then discharged to 2.5 V and further charged to 4.0 V. Figure 5 shows the selected ranges of the in situ XRD patterns and the cell parameters of NVCP at different charge/discharge states and the corresponding electrochemical curves. The whole ranges of the representing patterns can be found in Figure S5. Different from $Na_3V_2(PO_4)_3$ exhibiting a typical biphasic mechanism during the extraction/insertion of Na from/into the NASICON framework,[21] NVCP presents more complicated in situ XRD features according to which the patterns can be divided into six stages.

During stage I, as can be seen in Figure 5b, the Bragg peaks shift slightly toward higher angles, and the nearly negligible movement of the peaks indicates a single-phase reaction with subtle contraction of the unit cell of NVCP. Subsequently, the further extraction of Na causes the quick contraction of the unit cell, leading to the fast movement of the peaks toward higher angles at stage II. At stage III, the cell parameters and the peak positions are nearly constant. In the final stages (IV) of the charge process, *a*-axis decreases, whereas *c*-axis increases progressively. The elongation of the *c*-axis during the high-voltage charging process is very likely caused by the removal of

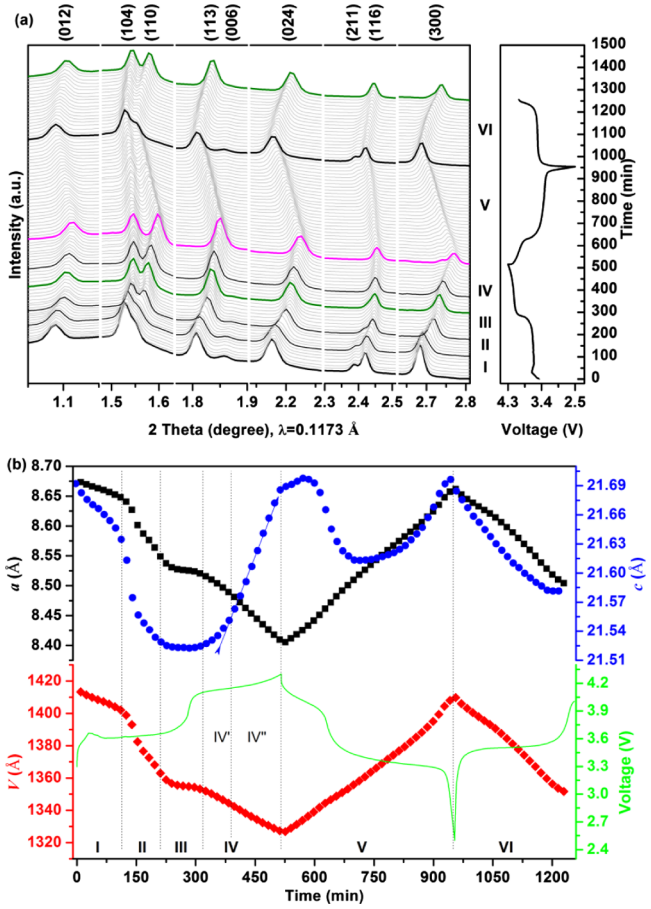

Figure 5. (a) In situ synchrotron XRD patterns of the NVCP electrode cycled at room temperature at 0.1 C between 2.5 and 4.3 V. (b) Evolution of the electrode lattice parameters during the first charge/discharge and partial second charge process, obtained by refining the XRD patterns. Charge/discharge curves are the inset in the figures.

Na from the Na(1) site because the depopulation of Na(1) would result in strong repulsions between the adjacent MO_6 (M = V or Cr) octahedral faces along [001], as can be seen in Figure 1b.[22] On the basis of these results, we suggest that Na at the Na(1) site is removed during the first charging process between 3.8 and 4.3 V. Furthermore, as indicated by the arrow in Figure 5b, stage IV can be divided into two substages, IV′ and IV″, based on the increased rate of the *c*-axis. Specifically, the *c*-axis elongates with lower and increased rates in stage IV′ and with a constant higher rate in stage IV″. Interestingly, the voltage at the starting point of stage IV″ is approximately 4.1 V, which agrees with the onset of the upper limit voltage that causes the degeneracy of the high-voltage capacity.

The patterns and cell parameters of the discharge process exhibit simpler features than that of the charge process. The positions of the peaks shift toward lower angles approximately linearly during the whole discharge process (stage V). The evolution of the cell parameters *a* and *V* also exhibit the linear feature during stage V. More importantly, as shown in Figure S5b, the diffraction peaks do not completely shift back to their original positions at the end point of discharge, revealing an irreversible phase transformation process during Na extraction/insertion. Regarding the second charge process, it is apparent that the pattern features are quite different from that of the first

DOI: 10.1021/acsami.7b13018
ACS Appl. Mater. Interfaces 2017, 9, 43632−43639

charge, meaning that irreversible transformation of the structure has occurred in the first charge process.

On the basis of the aforementioned analysis, we conclude that the irreversible bulk structure transformation coupled with the unrecovered local environment of vanadium atoms causes the loss of the high-voltage capacity, thus leading to the decrease of the overall capacity of deep desodiated NVCP during cycling. It is worth noticing that the irreversible transitions are possibly kinetically slow and that the desodiated species $Na_{2-y}V_y^{5+}V_{1-y}^{4+}Cr(PO_4)_3$ is metastable because the Na(1) site is immediately depopulated with the onset of the high-voltage plateau, whereas the NVCP electrode still shows good cycling stability when the upper cutoff voltage is 4.0 V, as shown in Figure S2. Thanks to the fast ion mobility of the NASICON-structured NVCP, we can further prove the hypothesis by cycling the NVCP electrode at higher current density (e.g., 1 C, Figure S6). As expected, the maintenance of the staircase features of the charge/discharge profiles and the capacity retention versus cycle number of NVCP cycled at higher rate are much better than that of the lower rate, which is highly similar to the phase transition of monoclinic Li_2FeSiO_4 cycled at different rates, as reported by Orikasa et al.[23] It is reported that monoclinic Li_2FeSiO_4 would completely transform to a thermodynamically stable orthorhombic $LiFeSiO_4$ upon the extraction of Li at a rate of C/50, whereas cycling at C/10 will lead to the retention of Li_2FeSiO_4 backing to the metastable monoclinic phase. Consequently, we preliminarily speculate that the deep desodiated species $Na_{2-y}V_y^{5+}V_{1-y}^{4+}Cr(PO_4)_3$ is metastable, which will slowly reconstruct into "low-voltage species" and/or inactive phases at 30 °C. Therefore, the phase changes would result in the variation of electrochemical features and the rapid loss of capacity of NVCP within a few cycles at the lower cycling rate at 30 °C. In this sense, suppressing the kinetics for the reconstruction process by lowering the test temperature might be an effective approach to improve the cycle life of NVCP, provided the fast ion mobility and excellent charge-transfer kinetics in the NASICON-structured NVCP.

Galvanostatic discharge/charge profiles at a 0.1 C rate of NVCP at −15 °C are shown in Figure 6a. The abnormal voltage steps highlighted by arrows could be attributed to the variation of the potential of the Na counter electrode in the PC/FEC electrolyte owing to the parasitic reactions between Na and the electrolyte in the coin cell.[16,24] The abnormal steps disappeared in the three-electrode cell, as shown in the inset in Figure 6b. In addition, the different plateaus of the NVCP cathode in the coin cell and the three-electrode cell are also caused by the different electrochemical test methods. The initial charge and discharge capacities of NVCP at −15 °C are 93 and 89 mA h/g, respectively, corresponding to an initial Coulombic efficiency of 96%, which is much higher than that at 30 °C (83%), indicating an enhanced reversibility at low temperature. Moreover, at −15 °C, the initial high-voltage and low-voltage discharge capacities correspond to 0.6-electron V^{4+}/V^{5+} and 0.9-electron V^{3+}/V^{4+} reactions in NVCP, respectively, leading to a 1.5-electron overall reaction per vanadium. In contrast to the commonly gained realization that low temperatures would severely lower the capacity of the electrodes,[25] NVCP shows nearly identical discharge capacity at −15 and 30 °C. Moreover, the staircase features of the profiles could be effectively preserved during cycling compared to that at 30 °C. Furthermore, as shown in the inset of Figure 6a, the retention of the discharge capacity of the cell cycled at −15 °C is as high

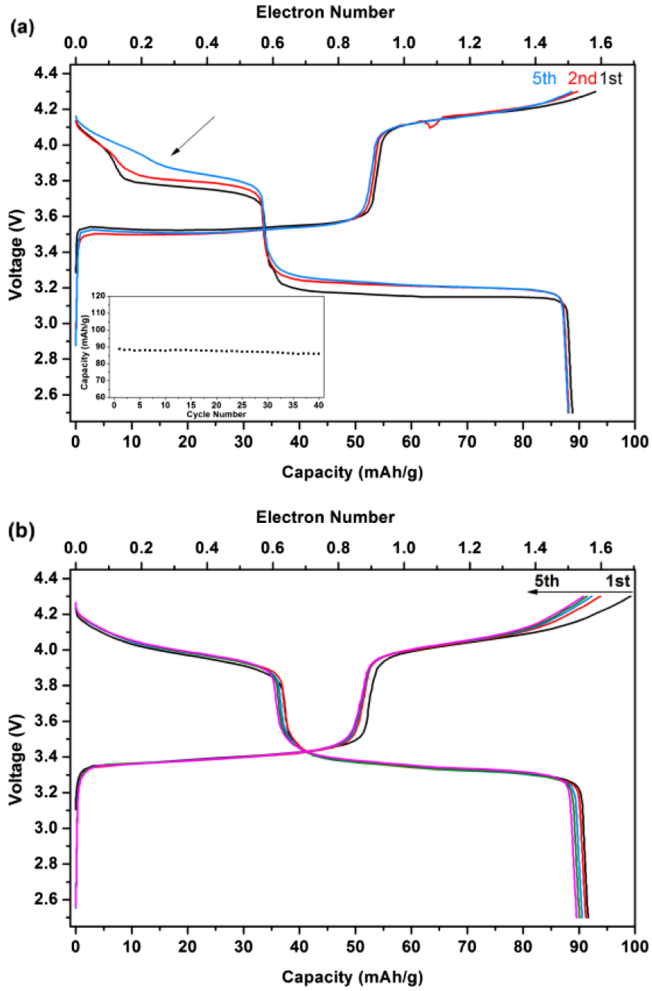

Figure 6. (a) Charge/discharge profiles of the NVCP coin cell and (b) three-electrode cell cycled at 0.1 C at −15 °C. The inset in (a) is the discharge capacity vs cycle number.

as 97% after 40 cycles. Figure S7 compares the Coulombic efficiency of NVCP cycled at −15 and 30 °C. It is evident that the cell exhibits better reversibility at −15 °C than that at 30 °C. Clearly, as shown in Figure S8, the improvements are mainly attributed to the improved reversibility and stability of the electrochemical reaction at high-voltage region. Briefly, the charge/discharge profiles of NVCP exhibit much more improved reversibility and stability cycled at −15 °C than that at 30 °C. Figure 7 demonstrates that NVCP demonstrates excellent cycling performance when cycled at −15 °C at 0.5 C. The initial discharge capacity (95%) at 0.5 C is still delivered after 200 cycles. The charge/discharge curves (Figure S9) also indicate that the high-voltage plateau and the low-voltage plateau are well-preserved during long cycling at −15 °C.

Ex situ XRD was performed to testify whether the structure of NVCP recovers to the original state after one cycle at 30 and −15 °C. With the help of the Al current collector as an internal indicator, we are able to compare the shift of the diffraction peaks reliably. As shown in Figure S10, the XRD patterns further demonstrate that the diffraction peaks do not recover after one cycle at 30 °C, in accordance with the in situ XRD data shown in Figure S5. Figures 8 and S11 show that all of the diffraction peaks shift to their original position after the first cycle, indicating a fully reversible sodium extraction and insertion process at −15 °C. It may suggest that a slight

DOI: 10.1021/acsami.7b13018
ACS Appl. Mater. Interfaces 2017, 9, 43632−43639

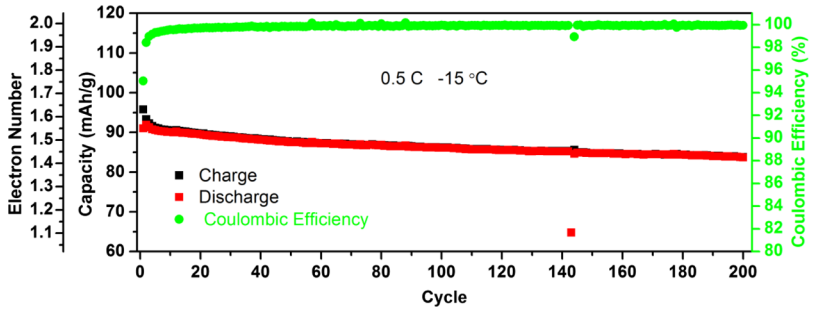

Figure 7. Cycling performances of NVCP cycled in a three-electrode cell at 0.5 C at −15 °C.

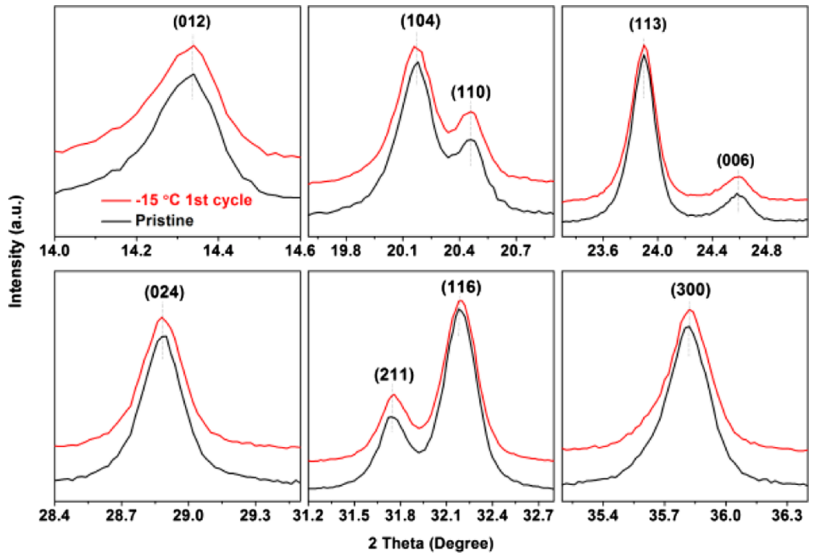

Figure 8. Selected ranges of ex situ XRD patterns of the pristine electrode and that cycled at −15 °C.

change in the local electronic/structural changes was suppressed at low temperature because of kinetic reasons when compared with the case at room temperature. Consequently, the recovered structural transition at −15 °C enables the reversible and stable 1.5-electron reaction per vanadium ion in NVCP. We anticipate that future efforts on the suppression of detrimental phase transformations using doping methods that are commonly adopted in layered transition-metal oxides might further stabilize the sodium extraction/insertion reactions at room temperature.[26−28]

CONCLUSIONS

We show that a 1.5-electron transfer could be achieved in a NASICON-type material NVCP. The redox couple V^{3+}/V^{4+} and V^{4+}/V^{5+} could be observed from a series of characterization techniques such as in situ XRD, ex situ solid-state NMR, and XANES. The mechanism of the capacity decay from the slight structural irreversibility with the formation of a metastable phase at the room temperature was also revealed by these characterization techniques. Besides, by suppressing the irreversibility at frozen temperature, we showed that the performance will be largely improved, with 92% retention after 200 cycles.

ASSOCIATED CONTENT

Supporting Information

The Supporting Information is available free of charge on the ACS Publications website at DOI: 10.1021/acsami.7b13018.

Atomic coordinates, morphology, charge/discharge curve at different rates, ex situ XAFS, and in situ XRD (PDF)

AUTHOR INFORMATION

Corresponding Author

*E-mail: yyang@xmu.edu.cn.

ORCID

Rui Liu: 0000-0001-6985-9129
Shiyao Zheng: 0000-0001-5002-5204
Riqiang Fu: 0000-0003-0075-0410
Zonghai Chen: 0000-0001-5371-9463
Khalil Amine: 0000-0001-9206-3719

Notes

The authors declare no competing financial interest.

ACKNOWLEDGMENTS

This work is financially supported by the National Key Research and Development Program of China (grant no. 2016YFB0901502) and the National Natural Science Foundation of China (grant nos. 21233004, 21428303, and 21621091). We also gratefully acknowledge the support from the U.S. Department of Energy (DOE), Vehicle Technologies Office. The Argonne National Laboratory is operated for DOE Office of Science by UChicago Argonne, LLC, under contract number DE-AC02-06CH11357. R.F. thanks the support from the Professional Development Leave Program at the Florida State University.

DOI: 10.1021/acsami.7b13018
ACS Appl. Mater. Interfaces 2017, 9, 43632−43639

REFERENCES

(1) Choi, J. W.; Aurbach, D. Promise and Reality of Post-lithium-Ion Batteries with High Energy Densities. *Nat. Rev. Mater.* **2016**, *1*, 16013.

(2) Ni, Q.; Bai, Y.; Wu, F.; Wu, C. Polyanion-Type Electrode Materials for Sodium-Ion Batteries. *Adv. Sci.* **2017**, *4*, 1600275.

(3) Fang, Y.; Zhang, J.; Xiao, L.; Ai, X.; Cao, Y.; Yang, H. Phosphate Framework Electrode Materials for Sodium Ion Batteries. *Adv. Sci.* **2017**, *4*, 1600392.

(4) Lalère, F.; Seznec, V.; Courty, M.; David, R.; Chotard, J. N.; Masquelier, C. Improving the Energy Density of $Na_3V_2(PO_4)_3$-Based Positive Electrodes through V/Al Substitution. *J. Mater. Chem. A* **2015**, *3*, 16198−16205.

(5) Wen, B.; Wang, Q.; Lin, Y.; Chernova, N. A.; Karki, K.; Chung, Y.; Omenya, F.; Sallis, S.; Piper, L. F. J.; Ong, S. P.; Whittingham, M. S. Molybdenum Substituted Vanadyl Phosphate ϵ-$VOPO_4$ with Enhanced Two-Electron Transfer Reversibility and Kinetics for Lithium-Ion Batteries. *Chem. Mater.* **2016**, *28*, 3159−3170.

(6) Gao, H.; Li, Y.; Park, K.; Goodenough, J. B. Sodium Extraction from NASICON-Structured $Na_3MnTi(PO_4)_3$ through Mn(III)/Mn(II) and Mn(IV)/Mn(III) Redox Couples. *Chem. Mater.* **2016**, *28*, 6553−6559.

(7) de Boisse, B. M.; Ming, J.; Nishimura, S.-I.; Yamada, A. Alkaline Excess Strategy to NASICON-Type Compounds towards Higher-Capacity Battery Electrodes. *J. Electrochem. Soc.* **2016**, *163*, A1469−A1473.

(8) Klee, R.; Lavela, P.; Aragón, M. J.; Alcántara, R.; Tirado, J. L. Enhanced High-Rate Performance of Manganese Substituted $Na_3V_2(PO_4)_3$/C as Cathode for Sodium-Ion Batteries. *J. Power Sources* **2016**, *313*, 73−80.

(9) Aragón, M. J.; Lavela, P.; Alcántara, R.; Tirado, J. L. Effect of Aluminum Doping on Carbon Loaded $Na_3V_2(PO_4)_3$ as Cathode Material for Sodium-Ion Batteries. *Electrochim. Acta* **2015**, *180*, 824−830.

(10) Aragon, M. J.; Lavela, P.; Ortiz, G. F.; Tirado, J. L. Effect of Iron Substitution in the Electrochemical Performance of $Na_3V_2(PO_4)_3$ as Cathode for Na-Ion Batteries. *J. Electrochem. Soc.* **2015**, *162*, A3077−A3083.

(11) Aragón, M. J.; Lavela, P.; Ortiz, G. F.; Tirado, J. L. Benefits of Chromium Substitution in $Na_3V_2(PO_4)_3$ as a Potential Candidate for Sodium-Ion Batteries. *ChemElectroChem* **2015**, *2*, 995−1002.

(12) An, Q.; Xiong, F.; Wei, Q.; Sheng, J.; He, L.; Ma, D.; Yao, Y.; Mai, L. Nanoflake-Assembled Hierarchical $Na_3V_2(PO_4)_3$/C Microflowers: Superior Li Storage Performance and Insertion/Extraction Mechanism. *Adv. Energy Mater.* **2015**, *5*, 1401963.

(13) Ravel, B.; Newville, M. ATHENA,ARTEMIS,HEPHAESTUS: Data Analysis for X-ray Absorption Spectroscopy Using IFEFFIT. *J. Synchrotron Radiat.* **2005**, *12*, 537−541.

(14) Lalère, F.; Leriche, J. B.; Courty, M.; Boulineau, S.; Viallet, V.; Masquelier, C.; Seznec, V. An All-solid State NASICON Sodium Battery Operating at 200 °C. *J. Power Sources* **2014**, *247*, 975−980.

(15) Saravanan, K.; Mason, C. W.; Rudola, A.; Wong, K. H.; Balaya, P. The First Report on Excellent Cycling Stability and Superior Rate Capability of $Na_3V_2(PO_4)_3$ for Sodium Ion Batteries. *Adv. Energy Mater.* **2013**, *3*, 444−450.

(16) Broux, T.; Bamine, T.; Fauth, F.; Simonelli, L.; Olszewski, W.; Marini, C.; Ménétrier, M.; Carlier, D.; Masquelier, C.; Croguennec, L. Strong Impact of the Oxygen Content in $Na_3V_2(PO_4)_2F_{3-y}O_y$ ($0 \le y \le 0.5$) on Its Structural and Electrochemical Properties. *Chem. Mater.* **2016**, *28*, 7683−7692.

(17) Serras, P.; Palomares, V.; Alonso, J.; Sharma, N.; del Amo, J. M. L.; Kubiak, P.; Fdez-Gubieda, M. L.; Rojo, T. Electrochemical Na Extraction/Insertion of $Na_3V_2O_{2x}(PO_4)_2F_{3-2x}$. *Chem. Mater.* **2013**, *25*, 4917−4925.

(18) Wong, J.; Lytle, F. W.; Messmer, R. P.; Maylotte, D. H. K-Edge Absorption Spectra of Selected Vanadium Compounds. *Phys. Rev. B: Condens. Matter Mater. Phys.* **1984**, *30*, 5596−5610.

(19) Dupré, N.; Gaubicher, J.; Guyomard, D.; Grey, C. P. ^{7}Li and ^{51}V MAS NMR Study of the Electrochemical Behavior of $Li_{1+x}V_3O_8$. *Chem. Mater.* **2004**, *16*, 2725−2733.

(20) Broux, T.; Bamine, T.; Simonelli, L.; Stievano, L.; Fauth, F.; Ménétrier, M.; Carlier, D.; Masquelier, C.; Croguennec, L. V^{IV} Disproportionation Upon Sodium Extraction From $Na_3V_2(PO_4)_2F_3$ Observed by Operando X-ray Absorption Spectroscopy and Solid-State NMR. *J. Phys. Chem. C* **2017**, *121*, 4103−4111.

(21) Jian, Z.; Han, W.; Lu, X.; Yang, H.; Hu, Y.-S.; Zhou, J.; Zhou, Z.; Li, J.; Chen, W.; Chen, D.; Chen, L. Superior Electrochemical Performance and Storage Mechanism of $Na_3V_2(PO_4)_3$ Cathode for Room-Temperature Sodium-Ion Batteries. *Adv. Energy Mater.* **2013**, *3*, 156−160.

(22) Masquelier, C.; Wurm, C.; Rodríguez-Carvajal, J.; Gaubicher, J.; Nazar, L. A Powder Neutron Diffraction Investigation of the Two Rhombohedral NASICON Analogues: γ-$Na_3Fe_2(PO_4)_3$ and $Li_3Fe_2(PO_4)_3$. *Chem. Mater.* **2000**, *12*, 525−532.

(23) Masese, T.; Orikasa, Y.; Tassel, C.; Kim, J.; Minato, T.; Arai, H.; Mori, T.; Yamamoto, K.; Kobayashi, Y.; Kageyama, H.; Ogumi, Z.; Uchimoto, Y. Relationship between Phase Transition Involving Cationic Exchange and Charge-Discharge Rate in Li_2FeSiO_4. *Chem. Mater.* **2014**, *26*, 1380−1384.

(24) Rudola, A.; Aurbach, D.; Balaya, P. A New Phenomenon in Sodium Batteries: Voltage Step Due to Solvent Interaction. *Electrochem. Commun.* **2014**, *46*, 56−59.

(25) You, Y.; Yao, H.-R.; Xin, S.; Yin, Y.-X.; Zuo, T.-T.; Yang, C.-P.; Guo, Y.-G.; Cui, Y.; Wan, L.-J.; Goodenough, J. B. Subzero-Temperature Cathode for a Sodium-Ion Battery. *Adv. Mater.* **2016**, *28*, 7243.

(26) You, Y.; Kim, S. O.; Manthiram, A. A Honeycomb-Layered Oxide Cathode for Sodium-Ion Batteries with Suppressed P3-O1 Phase Transition. *Adv. Energy Mater.* **2017**, *7*, 1601698.

(27) Zheng, S.; Zhong, G.; McDonald, M. J.; Gong, Z.; Liu, R.; Wen, W.; Yang, C.; Yang, Y. Exploring the Working Mechanism of Li^+ in O3-type $NaLi_{0.1}Ni_{0.35}Mn_{0.55}O_2$ Cathode Materials for Rechargeable Na-Ion Batteries. *J. Mater. Chem. A* **2016**, *4*, 9054−9062.

(28) Wu, X.; Xu, G.-L.; Zhong, G.; Gong, Z.; McDonald, M. J.; Zheng, S.; Fu, R.; Chen, Z.; Amine, K.; Yang, Y. Insights into the Effects of Zinc Doping on Structural Phase Transition of P2-Type Sodium Nickel Manganese Oxide Cathodes for High-Energy Sodium Ion Batteries. *ACS Appl. Mater. Interfaces* **2016**, *8*, 22227−22237.

DOI: 10.1021/acsami.7b13018
ACS Appl. Mater. Interfaces 2017, 9, 43632−43639